Cu- And Fe-speciation in a composite zeolite catalyst for selective catalytic reduction of NOx: insights fromoperandoXAS

Cu- and Fe-speciation in composite zeolite catalyst for selective catalytic reduction of NO_x: insights from operando XAS

Author list: Ilia A. Pankin[a,b], Houeida Issa Hamoud[c], Kirill A. Lomachenko[d]*, Søren Birk Rasmussen[e], Andrea Martini[a,b], Philippe Bazin[c], Valentin Valtchev[c], Marco Daturi[c]*, Carlo Lamberti[a,b]†, Silvia Bordiga [a,f]

Affiliation list:

a - Department of Chemistry, NIS Center and INSTM Reference Center, University of Turin, via P. Giuria 7, 10125, Turin, Italy
b - Smart Materials Research Institute, Southern Federal University, Sladkova Str. 174/28, 344090, Rostov-on-Don, Russia
c - Laboratoire Catalyse & Spectrochimie, ENSICAEN - Université de Caen – CNRS 6 Boulevard Maréchal Juin, 14050 Caen, France
d - European Synchrotron Radiation Facility, 71 Avenue des Martyrs, CS 40220 Grenoble Cedex 9, 38043, France
e - Haldor Topsøe, Haldor Topsøes Allé 1, 2800 Lyngby, Denmark
f - Center for Materials Science and Nanotechnology (SMN), Department of Chemistry, University of Oslo, 1033 Blindern, 0315, Oslo, Norway

Abstract: Cu-SAPO-34 (Cu-CZC) and Fe-Mordenite (Fe-MOR) and their mechanical mixture (50:50) have been exhaustively investigated by means of operando X-ray absorption spectroscopy under NH_3-SCR conditions. Fe K-edge XANES and EXAFS analysis revealed similar Fe-speciation in both pure Fe-MOR catalyst and the mechanical mixture after high-temperature pretreatment and under reaction conditions. In contrast, analysis of the Cu K-edge dataset unveiled essentially different trends in temperature-driven Cu-speciation in the pure Cu-CZC and mechanical mixture under standard NH_3-SCR conditions. This difference is more evident in the low-temperature range. The presence of Fe-MOR component in the mixed catalyst can result in the increase of NH_3 an NO concentration in proximity of Cu-sites at low temperature regime, which facilitates temperature-driven migration of NH_3-solvated mobile di-amino complexes from Cu-CZC to the MOR framework. This decreases the density of mobile Cu^I complexes in the entire system and results in the higher reducibility of Cu in the mixed catalyst. The obtained results help in understanding the precise speciation of the active sites in such composite catalysts and thus provides future guidance to design of such systems.

1. Introduction

NH_3-assisted Selective Catalytic Reduction (NH_3-SCR) catalyzed by metal-exchanged zeolites is a promising way to remove hazardous NO_x from diesel engine exhaust gases [1-5]. The development of after-treatment catalysts able to abate NO_x emissions, meeting the increasingly demanding air-quality EU standards, is an ongoing challenge, which nowadays attracts an enormous research interest from both academic and industrial laboratories, notably addressing the efficient zeolite-based SCR process[6].

The reason to investigate the bimetallic catalysts is provided by the fact that Fe-exchanged zeolites were found to be highly active at high temperatures (T > 350 ^oC), while Cu-zeolites demonstrate superior activity at low temperature SCR (T < 300 ^oC)[7-12]. In this regard, different complex system containing simultaneously copper and iron zeolites, such as dual-layer catalysts and Cu-Fe co-exchanged zeolites [8, 12-18] were thoroughly investigated in order to efficiently cover a broad temperature range. Moreover, additional interest to this kind of system is given by the fact that in few recent works the synergetic effect between Cu and Fe sites was proposed for different catalytic reactions. Hammond et al. [19, 20] reported an increase of the methanol selectivity for direct methane to methanol conversion over Fe-ZSM-5 catalysts caused by the presence of Cu^{II} cations in the catalyst. The Fe and/or Cu-containing BEA zeolites prepared by two-step post-synthesis

method and conventional wet impregnation have been studied for NH_3-SCR applications [21]. It was shown that the co-presence of copper in the zeolite structure decreased the reducibility of iron and had significant influence on the low temperature NO conversion. The Cu-Fe/ZSM-5 catalyst, prepared by subsequent ion-exchange, showed higher NO_x conversion compared with Fe/ZSM-5 or Cu/ZSM-5 due to the facile reduction of metal species [9]. The (Cu + Fe)-beta catalyst, prepared by solid-state ion-exchange method, showed higher NH_3-SCR activity over a broader temperature range, and especially at low temperature as compared to the Fe-beta and Cu-beta counterparts [13]. Gao et al. [12] exhaustively investigated catalytic activity and selectivity under NH_3-SCR conditions of the physical mixture of hydrothermally aged Cu-SSZ-13 and Fe-SSZ-13, revealing that such catalyst provide stable SCR performance in wide temperature range and essentially decrease N_2O formation at high temperature. Metkar et al. [7] showed that a dual layer with a thinner Fe-ZSM-5 layer on top of a thicker Cu-CHA layer at bottom gave maximum NO_x reduction activities for the fast SCR reactions. While great research efforts have been done on the investigation of Me-sites speciation in the monometallic exchanged zeolites under NH_3-SCR conditions, complete understanding of both structural and electronic properties of the metallic active Cu- and Fe-sites simultaneously present in the catalyst under SCR conditions is still an ongoing challenge. Furthermore, the synthesis of bimetallic zeolitic catalysts is a complex process which may involve few post-synthesis steps such as liquid and solid-state ion exchange or wet impregnation [9, 13, 21]. Therefore, we have recently proposed, as an alternative, the mechanical mixture of Cu and Fe-exchanged zeolites, which has shown superior catalytic performances respect to the average of the monometallic counterparts [22]. However, some questions remained open concerning the state of copper and iron inside the porous materials, as well as the synergy between the two cations (placed at a relatively long distance in the physical mixture, indeed) and the possible modification of the catalyst composition under stream. This requires a deeper insight into the chemical and physical properties of the materials during the catalytic action, which is the focus of the present study.

Recently the speciation of Cu-sites during high temperature pre-treatment and under NH_3-SCR conditions has been studied using a combined in situ UV-vis, FTIR and XAS spectroscopies [23-26], as well as by combining Cu K-edge XANES and XRPD Rietveld maximum entropy refinement [27]. Lomachenko et al. [28], based on combined experimental XAS and valence-to-core XES investigations of Cu-SSZ-13 (Cu:Al = 0.48; Si:Al = 15), revealed the co-presence of Cu^I/Cu^{II} species with the predominance of mobile NH_3-solvated complexes for low-temperature SCR (< ~200 °C), while higher Cu^{II} fraction can be obtained at higher temperatures (> 350 °C). Tyrsted et al. [29], also reported a nitrate-nitrite equilibrium on Cu-CHA catalysts by implementation of in situ FTIR, UV-vis and Cu K-edge XAS approaches.

Generally, the SCR reaction is sub-divided into standard SCR, which is the formation of nitrogen from NO and NH_3 without NO_2, and fast SCR, which happens in the presence of NO_2 [30]. A consequence of the NH_3-SCR reaction scheme proposed by Janssens et al., [23] assumes that all intermediates in fast SCR are also part of the standard SCR cycle. Moreover, the activation energy obtained by DFT indicates that the oxidation of NO molecule by O_2 to a bidentate nitrate ligand is rate-determining for standard SCR [23]. More recently, Paolucci et al., [31] proposed a new mechanism of Cu sites speciation under low-temperature NH_3-SCR conditions. The catalysts with different Cu loading have been examined using in situ XAS spectroscopy accompanied by DFT and *ab initio* molecular dynamics. The authors proposed that NH_3-solvated mobile Cu^I complexes with a mobility restricted by electrostatic interaction with Al in a framework T-sites are able to reversibly form NH_3-coordinated dimers via activation of oxygen molecules [31]. In parallel, similar mechanism, that links homo- and heterogeneous catalysis has been proposed by Gao and co-workers [32].

The variety of different active Fe-sites in the Fe-exchanged zeolites is even higher assuming also a possible formation of iron oxide cluster detected by UV-vis and FTIR spectroscopies in several works [33-38]. The formation of monomeric and dimeric iron species in Fe-ZSM-5 catalyst under different pre-treatment conditions have been discussed on the basis of Fe K-edge EXAFS analysis [39]. Based on the lack of Fe-Fe contribution and the presence of Fe-Al contribution resulting in a coordination number around 1, Choi et al., proposed the formation of monomeric Z-[$Fe(O_2)$]$^+$ and Z-[$Fe(OH)_2$] as a dominant iron site under He or CO atmosphere. Such species are almost unaffected by the Fe:Al ratio.

Forde et al. [35] demonstrated the Fe-Fe contribution to the EXAFS signal has been found for Fe-ZSM-5 and Cu-Fe-ZSM-5 catalysts with Fe loading *ca.* 4% calcined at 550 ^oC in air. The authors proposed the formation of iron oligomers with a Fe^{3+}/Fe^{2+} in octahedral coordination or a small Fe_2O_3 cluster. The critical iron loading to form an isolated iron species inside the zeolites was reported to be around 0.2 wt% of Fe [40]. However, this value may vary depending on framework topology (i.e. pore size and availability) and Si/Al ratio. Maier et al. also showed an effect of Fe loading on the abundancy of Fe_2O_3 oxides in a series of Fe-BEA catalysts via ex situ Mössbauer characterization [41].

In the same work the authors revealed reversible redox process occurring on the iron sites in Fe-BEA with 0.99 wt. % of Fe treated under nitrogen using operando Fe K-edge XANES. Earlier, the redox dynamics of Fe sites has been also investigated by EPR and optical spectroscopy [37, 38]. Also, numbers of studies have been done to investigate Fe-ZSM-5 catalysts by means of XAS proposing that the active sites are represented by di-nuclear iron oxo-/hydroxo cluster or an oligomeric iron-oxo species [42-45].

In the present work the Cu-CZC and Fe-MOR monometallic catalysts were selected for a XAS operando study due to their superior de-NO_x activity respectively at low and high-temperatures, as shown in our previous work [22]. Both Cu- and Fe-speciation in monometallic catalysts and their mechanical mixture were investigated by means of XANES and EXAFS analysis. Particular attention has been given to Cu-speciation in the mixed system, since it demonstrated very different behavior with respect to the monometallic counterpart. The formation of different mobile and framework-interacting Cu species under NH_3-SCR conditions has been quantitatively analyzed through principal component analysis (including advances statistical analysis) and further linear combination fit. Several hypotheses intended to explain the catalytic results and the mechanisms of the different Cu-speciation behavior in the monometallic and mixed catalysts have been proposed and critically discussed relying on the previously reported studies of SCR mechanism and ion migration processes in zeolites.

2. Experimental

2.1 Material description and methods

Protonated and copper exchanged silicoaluminophosphates (SAPO-34), CHA-type zeolites, were directly used as received from Clariant company. Commercial Mordenite (Si/Al = 6.2, Na^+ form) was received from Zeolyst. The Fe-containing mordenite, abbreviated as Fe-MOR, was prepared by the conventional ion exchange procedure [22]. In the first step, 1 g of parent MOR was mixed with 40 mL of aqueous solutions containing 0.05 M of $Fe(NO_3)_3 \cdot 9H_2O$ stirred at T = 60 °C for 4 h. The obtained suspensions were centrifuged, washed thoroughly with deionized water, freeze-dried for 2 nights and then calcined at 500°C for 4 h. The ion-exchange procedure was repeated

three times. The metal exchanged forms of monometallic zeolites are further abbreviated as Cu-CZC and Fe-MOR. Despite of the fact that typically Al-substituted CHA (i.e. SSZ-13) demonstrates better hydrothermal stability than Cu-SAPO-34 (Cu-CZC), stability of the latter can be significantly enhanced for the materials with smaller crystallite size and low Cu concentration on the crystal surface [46]. On the other hand, utilization of Fe-MOR is motivated by the fact that Fe-MOR effectively eliminates N_2O and exhibits high activity and excellent stability under practical conditions of NH_3-assisted SCR.

The sample of bimetallic catalyst, containing both Cu- and Fe-exchanged zeolite has been prepared by a simple mechanical mixing of two equal fractions of the above-mentioned components (0.5Cu-CZC + 0.5Fe-MOR) and further abbreviated as Cu-Fe-mix sample. The mixture was meticulously grounded in chemical mortar to promote a better mixing and close contact between the different zeolite grains.

The objects investigated in the present work through operando XAS experiment were previously exhaustively characterized by laboratory in situ FTIR as well as UV-vis spectroscopies [22]. Specific surface area was analyzed by BET technique performed within an ASAP 2020 MP analyzer. N_2 adsorption/desorption isotherms were collected at 77 K. The samples were degassed in situ at 350 ^oC for 3h prior to the measurements. The precise chemical composition of the samples was analyzed by ICP (Inductively Coupled Plasma) analysis. The Varian ICP-OES 720-ES spectrometer was employed to determine the contents of Si, Al, Cu and Fe in the samples.

2.2 XAS operando experiment details

Cu and Fe K-edge X-ray absorption near-edge structure (XANES) and extended X-ray absorption fines structure (EXAFS) spectra were measured at BM23 beamline of the European Synchrotron Radiation Facility (ESRF, Grenoble, France) [47]. A Si(111) double-crystal monochromator was used for energy scanning, whereas harmonics rejection was done by two flat Si mirrors positioned at 2.8 mrad. Incident and transmitted X-ray intensities were measured by three ionization chambers with gas filling acceptable for both Fe and Cu K-edges. The spectrum of Cu or Fe foil was collected simultaneously with each spectrum of the sample at the corresponding edge to ensure the energy calibration. XAS data reduction and XANES linear combination analysis were carried out in Athena, whereas EXAFS fitting was done in Artemis, both codes being part of Demeter package [48].

The powdered samples of monometallic catalysts have been prepared in the form of self-supporting pellets with the mass optimized for optimal signal-to-noise ratio that were computed within XAFSmass code [49]. The optimal mass for Cu-CZC is 109.3 mg, while for high-loaded Fe-MOR the optimal adsorption step could be achieved for the pellet mass of 38 mg. For mechanical mixture (Cu-Fe-mix), the optimized mass equal to 86.5 mg (43.25 mg for each component) was utilized as compromise in order to get appropriate absorption step both for Cu- and Fe- K-edges. The pellets were fixed inside the Aabspec CXX (ultra-low volume flow-through) reactor cell, initially dedicated to operando IR measurements and further customized for operando XAS measurements by substituting the standard KBr windows by Kapton ones. The cell belongs to the class of ultra-low volume flow-through cells that are very suitable for catalytic experiments.

The SCR experiment has been designed to carry out the same reaction under synchrotron beam and in a laboratory, by using the same Aabspec CXX 800 ^oC reactor-cell. The activation was performed by heating the samples from RT to 500 ℃ under 10 % O_2/He flow with a ramp rate of 5 ℃/min. Cu and/or Fe K-edge EXAFS data were collected at 200 ℃ and at 500 ℃ (*ca.* 20 min/scan). After the activation, EXAFS spectra were measured at fixed temperatures in the range

from 450 °C to 150 °C with the step of 50 °C under the NH_3-SCR conditions: 500 ppm NO, 500 ppm NH_3, 10% O_2, 2% H_2O balanced in He, with 100 ml/min total flow rate. The temperature ramp both upon the activation and transitions between the temperature points in SCR conditions were followed by faster XANES acquisitions (ca. 7 min/scan). For each temperature point along SCR ramp the EXAFS spectra have been taken for steady-state conditions after the stabilization of the system continuously monitored by XANES.

Importantly, Fe and Cu K-edge spectra for the mixed bimetallic sample were collected in a single run using the same pellet (thus making the dwell time at each temperature point roughly twice as long compared to the single-metal samples). Catalytic activity of the samples was evaluated simultaneously with XAS data acquisition by monitoring the effluent gas composition by an online mass spectrometer (Balzers Prisma). Activity of the samples was calculated using the NO signal (m/z = 30) corrected for MS drift using He signal (m/z = 4). The conversion data are reported in Section 3.2. Reported values were calculated as a difference between the outlet and inlet MS signal, preliminary normalized by He signal level:

$$Conversion\ \% = \frac{NO_{inlet} - NO_{outlet}}{NO_{inlet}} \cdot 100\% \quad (eq.1)$$

3. Results

3.1 Preliminary characterization

The physicochemical properties of the monometallic Cu-CZC and Fe-MOR catalysts and corresponding parent not-exchanged MOR zeolite were first investigated using XRD, N_2 physisorption at 77 K, ICP and FTIR in-situ spectroscopies. The results are summarized in Table **1**.

The ICP analysis shows that the copper and iron contents are about 1.56 wt. % of Cu and 7.55 wt. % of Fe for Cu-CZC and Fe-MOR samples, respectively. Corresponding (P+Al):Si and Cu/Si molar ratios are 11.2 and 0.44, respectively. The Si/Al molar ratio slightly increase after iron exchange of MOR framework, indicating a moderate decrease of framework Al content.

The PXRD patterns of the non-exchanged and metal exchanged zeolites are shown in Figure S2 of SI. It confirms that chabazite and mordenite crystal structures are maintained well after metal exchange. Only slight decrease in the reflection intensity was observed for Fe-MOR. This result can be related to the partial loss of framework crystallinity and to the absorption of X-rays by inserted metal ions, especially for high-loading Fe-MOR (See FigureS2 of SI). It should be noted that no traces of M_xO_y (M = Cu, Fe) oxide or metallic phases were detected in Cu-CZC and Fe-MOR patterns, suggesting that the metal species exist in highly dispersed states or they form some very small clusters that are beyond the detection limit of laboratory PXRD.

The BET surface area of Cu-CZC and Fe-MOR sample is around 568 m^2/g and 483 m^2/g, respectively. The iron loading in MOR structure causes a slight increase in BET surface areas and micro porosity likely due to the elimination of residual impurities in MOR micropores during washing steps. The total acidity and density of Lewis and Brønsted acid sites in the investigated catalysts has been determined by in situ FTIR after exposure to pyridine as reported in our previous study [22]. The data confirmed that copper remained a marginal Brønsted acidity in the Cu-CZC sample (0.11 μmole/g) with an additional Lewis acidity (17.8 μmol/g). The later remained accountable on Cu-CZC after desorption beyond 150 °C, indicating the presence of strong acidic sites in this sample. The concentration of Lewis acid sites was 64.7 μmol/g for Fe-MOR. An increase in the Lewis acidity took place when the temperature increased from 100 to 350 °C over

Fe-MOR, suggesting that some Lewis acid sites of medium-high strength could be recovered during the thermo-decomposition of pyridine [22].

Table 1. Summary of physochemical properties of the parent and metal exchanged zeolites.

Catalyst label	(Al+P)/Si	Cu/Si	M content*(wt. %)	S_{BET} (m^2/g)	V_{mic}(cm^3/g)
Cu-CZC	11.24	0.44	1.56	568	0.19
Catalyst label	**Si/Al**	**Fe/Al**	**M content*(wt. %)[a]**	**S_{BET}(m^2/g)**	**V_{mic}(cm^3/g)**
MOR parent	6.30	-	-	453	0.15
Fe-MOR	6.60	1.43	7.55	483	0.17

* as obtained from ICP analysis

3.2 Catalytic performance

The catalytic activity of the samples was monitored upon operando XAS experiment by online MS spectrometry as described in Section 2.2. NO conversion data measured upon operando XAS experiment are reported in Figure 1(a). Because of the differences in experimental conditions with respect to the previously reported laboratory results for the investigated samples[22], we have repeated catalytic experiment in the lab using the mass of the catalysts and total flow rate similar to those employed during operando XAS experiment. Corresponding data are reported as dashed curves in Figure 1. One can notice an excellent agreement between conversion rates obtained during the operando XAS experiment at the synchrotron and those re-measured in the lab. Moreover, since weights of the catalysts were optimized in order to have the best XAS signal above both Cu and Fe K-edges we introduced additional corrections. Figure 1(b) reports corrected NO conversion data for the two catalytic experiments that account for different catalysts mass and relevant reaction condition (i.e. GHSV = 50 000 h^{-1}), as detailed in Section 1 of SI.

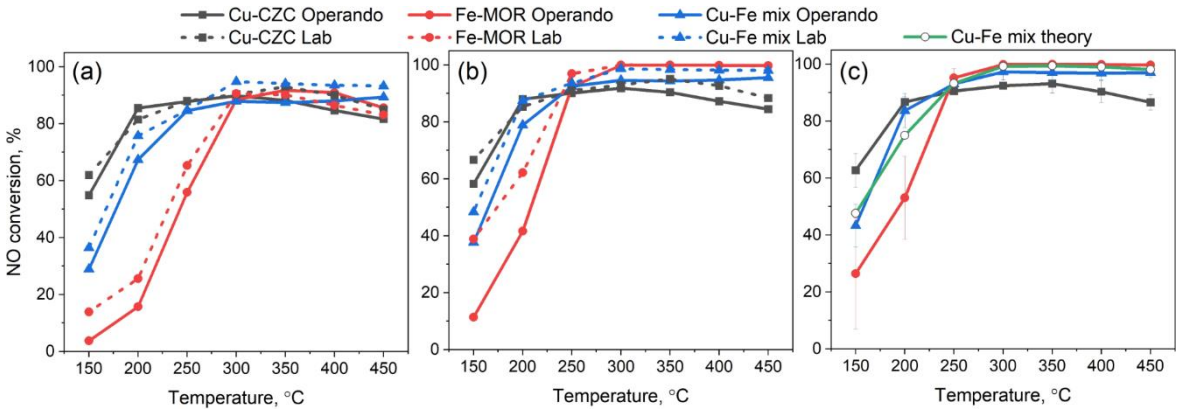

Figure 1 (a) NO conversion measured for Cu-CZC, Fe-MOR and their mechanical mixture during operando XAS experiment and in the lab with similar mass of the catalyst pellets and total flux. **(b)** NO conversion data recalculated for relevant reaction conditions (GHSV = 50 000 h^{-1}) as detailed in Section 1 of SI **(c)** Experimental NO conversion curves recalculated using the kinetic constants averaged over operando XAS and laboratory experiments together with the theoretical curve (green curve) simulated for the mixed material for the case when its Cu-CZC and Fe-MOR components work independently

ıd Fe-exchanged zeolites represents a compromise solution being highly effective at both low and high temperature SCR. Indeed, from Figure 1(b) it is clear that in the low temperature range the conversion rate observed for mechanical mixture is competitive with those obtained for pure Cu-CZC catalyst. Furthermore, as it was shown by Gao and co-workers, the presence of Fe-exchanged component may lead to decrease in N_2O release [12, 36], improving the selectivity of mixed catalysts in high temperature range with respect to single-component Cu-CZC catalyst.

However, it should be noted that a nearly 100 % selectivity for all the studied samples was observed in our recently published laboratory experiments [22], in particular no N_2O was detected. That agrees well with the linear dependence of N_2 vs NO conversion observed for all 3 catalysts in the current operando XAS study (See Figure S1 of SI).

Figure 1**(c)** shows the experimental NO conversion curves recalculated using the kinetic constants averaged over the two experiments (operando XAS and laboratory ones) in comparison with the theoretical curve simulated for the mixed material for the case when its Cu-CZC and Fe-MOR components work independently. One can clearly observe that at 200 ^oC the experimental catalytic activity obtained for Cu-Fe-mix sample exceeds the conversion rate expected from the mixture of non-interacting components. This observation is in line with the synergetic effect observed for Cu-Fe-mix sample in our previous work [22].

Aiming to shed light on the origin of such catalytic properties, we investigated Cu and Fe speciation in the single-component Cu-CZC, Fe-MOR and their mechanical mixture during activation and under reaction conditions by X-ray absorption spectroscopy.

3.3 Fe-speciation upon activation and SCR

Figure 2 reports Fe K-edge XANES spectra collected for Cu-Fe-mixed sample under steady state conditions upon the activation in air at RT, 200 ^oC and 500 ^oC in comparison with the data collected on the iron oxide α-$Fe(III)_2O_3$ (hematite phase). The features around the main threshold of XANES spectrum are associated with 1s→4p dipole transitions, while the small peak in the pre-edge region is assigned to transitions from 1s to 3d-4p hybridized states caused by non-centrosymmetry of the Fe species, as well as to quadrupole (dipole forbidden) 1s→3d transitions [50, 51].

The results show that the Fe K-edge XANES spectra of the mixture at RT exhibit a very similar shape to α-Fe_2O_3 oxide, and thus probably Fe species in the investigated sample have very similar local atomic environment, to the one observed for the bulk α-Fe_2O_3 oxide (hematite). However, since no traces of this oxide phase were detected by PXRD, most of the iron atoms likely form very small Fe-O atomic clusters. The activation process is accompanied by a small gradual decrease of the main maximum intensity as well as an energy shift of the absorption threshold towards the lower energy, reflecting some weak temperature-induced structural rearrangements upon activation.

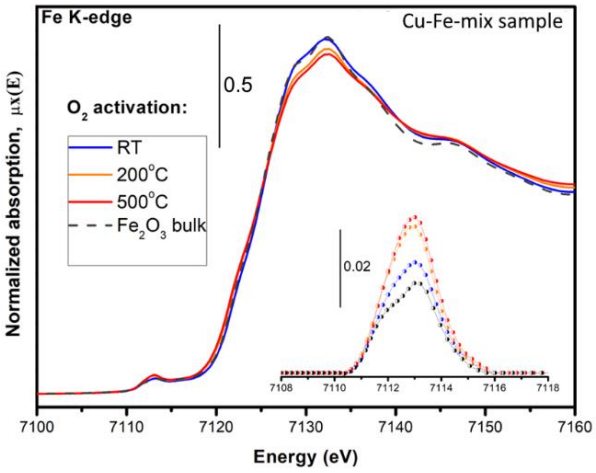

Fig. 2 Fe K-edge XANES spectra collected for Cu-Fe-mixed sample under steady-state conditions at RT, 200 ^oC and 500 ^oC upon the activation in oxygen in comparison with the data collected on the bulky iron oxide α-$Fe(III)_2O_3$ shown as a dashed curve. The inset show magnification of background subtracted pre-edge peak.

The inset of Figure 2 shows magnified background subtracted pre-edge peak intensity along the activation process. The intensity of the pre-edge peak increases with heating from RT to 500 °C, thus indicating an increase of the abundance of Fe-sites in T_h coordination as it was suggested in literature for Fe-MOR with different Fe loading[52] or due to the distortion of the O_h sites upon heating. Likewise, non-ideal average octahedral coordination of the Fe species in the sample before activation could be a reason of higher pre-edge peak intensity observed at RT with respect to α-$Fe(III)_2O_3$, where Fe-sites are supposed to have almost perfect octahedral coordination O_h^{3+}. Thereby it could be considered as an evidence of a small Fe-O clusters formation with highly defective structure of α-Fe_2O_3 due to the size effect. The formation of the dominant fraction of Fe-O clusters with a local atomic structure similar to γ-Fe_2O_3 (Maghemite) or Fe_3O_4 (Magnetite) is excluded because of mismatch of the experimental XANES signal obtained for the activated sample with the spectra of γ-Fe_2O_3 and Fe_3O_4 reported elsewhere [53]. Fe K-edge XANES collected for Fe-MOR upon activation demonstrate very similar trends and reported in Figure S13 of SI.

A further structural refinement of the small Fe-O clusters suggested to be formed both in monometallic Fe-MOR and Cu-Fe-mixed samples, was performed by means Fe K-edge EXAFS Fourier analysis. The k^2-weighted FT-EXAFS amplitudes obtained for Cu-Fe-mixed sample upon activation process under steady state conditions at RT, 200 °C and 500 °C are reported in Figure 3 (top part), while the temperature evolution of the EXAFS signal upon NH_3-SCR condition reported in Figure 3 (bottom part).

The qualitative examination show that the main features in EXAFS amplitudes obtained for Cu-Fe-mixed sample upon activation correspond to α-Fe_2O_3 bulk oxide phase. The intensity of the 1st coordination shell maximum (denoted as peak A at Figure 3, top) obtained for the catalyst at RT is slightly lower compared to α-Fe_2O_3. However, significantly more essential decrease of the 2nd and 3rd FT-EXAFS maxima intensity (denoted as peak B and C at Figure 3, top) can be observed. This could be associated with the size effect for a small Fe-O clusters formed in the catalyst. Indeed, significantly more damped oscillation in the extended post-edge region of the normalized XANES signal (See Figure S17 of SI) confirms strong particle size-effect.

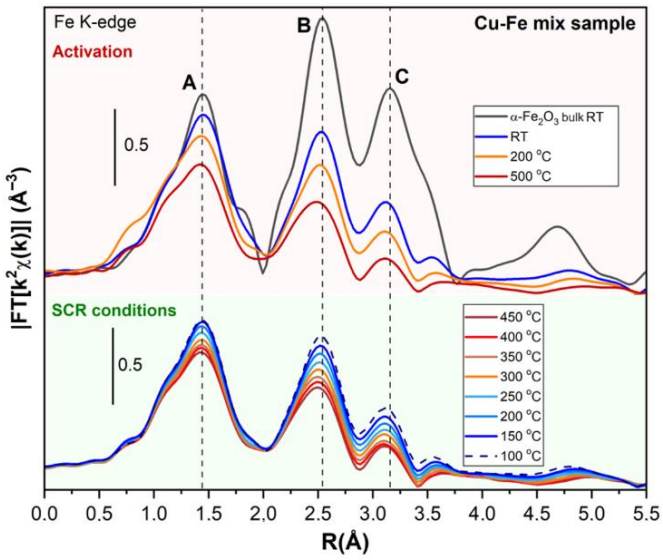

Fig. 3 Fe K-edge Fourier transformed phase uncorrected amplitudes of k^2-weighted experimental EXAFS signal collected for bimetallic Cu-Fe-mix upon high temperature O_2-activation (top part) and under NH_3-SCR reaction condition in a wide temperature range (bottom part) in comparison with the data collected at ambient conditions for bulk α-Fe^2O^3 phase. The vertical dashed lines correspond to the peak positions for α-Fe_2O_3.

The temperature evolution of the Fourier Transformed EXAFS amplitudes collected on Cu-Fe-mixed sample during activation and SCR conditions is accompanied by the gradual damping of the EXAFS signal. Qualitatively the observed trends assume almost no changes in the average local atomic structure in the proximity of iron sites upon activation (See Figure 3, top) and under SCR conditions (See Figure 3, bottom), while the decrease of the intensity upon temperature increase under SCR is related with the temperature effect on the EXAFS signal.

To get quantitative estimation of the changes observed between the samples and α-Fe_2O_3 bulk oxide as well as changes caused by temperature-driven evolution upon activation, the EXAFS fit was performed. Due to the similarities of EXAFS amplitudes obtained for investigated samples and α-Fe_2O_3 [54] (American Mineralogist database, str. № 0000143), the latter has been used as an initial guess for the fit. To emphasize a different behaviour of the first and higher coordination shells, we have performed EXAFS-analysis in the R-range from 1.1 to 3.5 Å, thus capturing the 2nd and 3rd peaks of experimental FT-EXAFS amplitudes. All SS and MS paths contributions within the effective path lengths up to 4.2 Å have been accounted for the fit. Different SS and MS paths were parameterized by scaling coefficients *n1*, *n2* and *n3* intended to describe CNs of the first (*n1*) and higher coordination shells (*n2*, *n3*). More details on EXAFS fit parametrization are reported in Section 3 of SI.

First, EXAFS fit of the experimental data collected on bulk iron oxide α-Fe_2O_3 was performed in order to get reliable value for passive amplitude reduction factor S_0^2, that was further fixed for all subsequent fits. In spite of the well-defined structural parameters of model compound (α-Fe_2O_3) the coordination numbers (i.e. *n1, n2, n3* coeff.) and displacement parameters ΔR_i have been set as fit parameters to provide more reliable structural parameters refinement for the catalysts under study. The fit results for oxide phase α-Fe_2O_3, Fe-MOR and Cu-Fe-mix samples at RT (before the activation) are reported in Table 2.

Table 2. The fit results reported for Fe K-edge k^2-weighted FT-EXAFS amplitudes obtained for bulk oxide phase α-Fe_2O_3 as well as Fe-MOR and Cu-Fe-mix catalysts at RT. The variables that have been fixed upon fit procedure are underlined. *an averaged cluster diameter <D> was estimated by using Calvin's model [55, 56] (see eq. 2) while the other fit parameters obtained by using this approach are reported in Table S2 of SI.

Fit parameters	**α-Fe_2O_3**	**Fe-MOR**	**Cu-Fe-mix**
ΔE (eV)	-4.026	-2.781	-2.338
N_{ind}/N_{par}	17.6 / 11	17.6 / 10	17.6 / 10
S_0^2	0.799	0.799	0.799
R-factor	0.003	0.003	0.002
Reduced χ^2	67.132	188.227	139.939
n_1	**0.92** ± 0.06	**0.93** ± 0.05	**0.92**±0.05
n_2	**1.02** ± 0.06	**0.78** ± 0.07	**0.79**±0.06
n_3	**0.84** ± 0.10	**0.47** ± 0.09	**0.49**±0.09
ΔR_O_1 (Å)	-0.015±0.005	-0.020±0.008	-0.021±0.007
ΔR_O_2 (Å)	-0.029±0.008	-0.048±0.009	-0.051±0.009
α (Å)	-0.0050±0.0030	-0.0007± 0.0031	-0.0008±0.003
$\sigma^2\_O_1$ (Å^2)	0.002±0.001	0.005 ± 0.001	0.004± 0.001
$\sigma^2\_O_2$ (Å^2)	0.003± 0.001	0.006 ± 0.002	0.006±0.002
σ^2_far (Å^2)	0.003± 0.001	0.005 ± 0.001	0.006±0.001
<D> (nm.)*	n/d	2.20±0.73	2.24±0.75
highest correlations	no correlations higher than 0.90	σ^2_far/n_2=0.930	no correlations higher than 0.90

Unlike the case of first oxygen shells characterized by the very similar CNs (i.e. similar values for *n1* scaling coefficient) both for α-Fe_2O_3 and investigated samples, a great discrepancy for *n2* and *n3* CNs scaling coefficients was obtained (See Table 2 and Figure S3 of SI). EXAFS fit yields significantly lower *n2* and *n3* values for Cu-Fe-mix sample reflecting a drastic decrease of the CNs for higher coordination shells (Coordination numbers for the selection of several strongest SS paths are reported explicitly in Table S1 of SI). This reduction of CNs is clearly caused by the

small size of Fe_2O_3 oxide clusters formed in both samples. Along with CNs reduction the small decrease in the distances by ~ 0.01 Å and ~ 0.02 Å (See Table 2), obtained for the first two oxygen sub-shells, supports the idea of small cluster size. DW factors obtained for Cu-Fe-mix and Fe-MOR samples are significantly higher with respect to those refined for α-Fe_2O_3, reflecting significantly higher disorder in local atomic structure of Fe-O clusters formed in the catalyst. Nevertheless, the good fit quality (R-factor = 0.0025 and 0.0029 for Cu-Fe-mix and Fe-MOR RT dataset, respectively) confirms that local atomic structure of small Fe-O clusters is very similar to the short-range atomic order in bulk hematite α-Fe_2O_3. The obtained result in a good agreement with those reported in ref [57], where the formation of hematite NPs in highly loaded Fe-BEA (5.1 wt. % of Fe) was revealed by UV-vis and EXAFS analysis.

Afterwards the experimental FT-EXAFS amplitudes collected for Cu-Fe-mixed sample at 200 °C and 500 °C were analyzed with a fixed scaling coefficients *n1*, *n2*, *n3* as obtained for RT fit. As expected, higher temperature EXAFS fits characterized by further essential increase of DW factors, providing a good fit quality reflected in very small R-factors both for 200 °C and 500 °C (0.003 and 0.004, respectively; See Table S3 of SI). The same trend is observed for the EXAFS fit of the data collected under SCR condition – the difference observed in the signal might be reliably associated mostly with temperature effect (See Table S3 and Figure S4 of SI).

Since no traces of iron oxide phases have been found in PXRD patterns acquired for single-component Fe-MOR sample (See Figure S2 of SI) the size of the Fe-O clusters is supposed to be less than laboratory X-ray diffractometer detection limit. To estimate the size of Fe-O clusters formed in the catalysts we have parametrized CNs in accordance with Calvin's model accounting for averaged particle size (roughly assuming for a spherical shape of the cluster) as described elsewhere [55, 56]:

$$N_i^{clust.} = \left[1 - \frac{3}{2}\frac{R_i}{D} + \frac{1}{2}\left(\frac{R_i}{D}\right)^3\right] N_i^{bulk} (eq. 2)$$

where N_i is the coordination numbers of *i*-scattering path (in cluster and in bulk materials, in accordance with the upper index), R_i– is the effective path lengths (in Å), D is the mean cluster diameter (in Å). This approach yields an averaged cluster's size to be equal to 2.24±0.75 nm for the Cu-Fe-mixed catalyst and even slightly lower (2.20±0.73 nm) for monometallic Fe-MOR (See Table 2). The all fit results obtained by means Calvin's model (*i.e.* eq. 2) is reported in Table S2 and Figure S3 of SI.

In fact, in case of broad distribution of the particle size this approach results in the size weighted toward the low part of the distribution [55]; thus the real averaged size of the clusters could be slightly larger and it implies that most of the Fe-O clusters are likely formed on the exterior surface of MOR crystals. This is in line with BET analysis, since even for highly loaded Fe-MOR the decrease in specific surface area after ion-exchange were not observed (See Table **1**), suggesting that no relatively big Fe agglomerates are formed inside MOR cavities.

To sum up, obtained on the basis of XANES and EXAFS analysis results declare that most of the Fe atomic species in the both catalysts are involved in the formation of very small iron clusters with local atomic structure similar to α-Fe_2O_3 oxide phase. However, analysis of the differential XANES signal reported in Figure S5 of SI allow to catch some tiny differences in Fe speciation. Taking into account that no appreciable structural differences was declared by means of EXAFS fit for high and low temperature datasets, the changes observed by differential XANES could be associated with the trace of minority of the isolated Fe-species.

Particularly the decrease of differential XANES signal observed for high temperature data (T > 350 °C) could be associated with the involvement of isolated Fe sites into redox chemistry at high temperature. Indeed, from previously reported catalytic activity for Fe-exchanged zeolites with moderate Fe-loading (that is not implying a favorable condition for Fe clusterization), the onset of de-NO_x activity is observed at 300-400 °C [9, 12, 36].

This fact reinforces our hypothesis about minority of isolated Fe-species that are being involved in redox chemistry at higher temperature likely form similar intermediates. This would result to the same averaged oxidation state and coordination environment of isolated Fe sites, thus damping differential XANES signal. It can be explained by the formation of some ammonia or water solvated iron complexes at high T under SCR conditions or due to hydrothermal aging [58, 59].

The interpretation of differential XANES evolution are supported by the findings of statistical and PCA analysis performed on Fe K-edge dataset (See Section 5.2 of SI). Importantly, the abstract components derived by using statistical analysis implemented in PyFitit package[60] closely resemble the differential XANES obtained for temperature induced evolution in Fe-MOR and the one obtained as a differential signal between Fe-MOR and Cu-Fe-mix samples after high-temperature O_2-activation (See Figure S9 of SI). Thus, differential XANES signal can be more reliably associated with the presence of minority of the isolated Fe-sites in the catalysts. However, the good quality of the EXAFS fit obtained on the basis of distorted α-Fe_2O_3 structure assume very low relative abundancy of the isolated Fe-sites, that is in a good agreement with very low dispersion (4%) of the isolated Fe-sites obtained by IR [22].

Summarizing, we suggest that iron sites in both pure Fe-MOR and two-component Cu-Fe-mix samples are represented by two main categories: small Fe_2O_3 clusters most likely deposited on the exterior MOR surface and the minority of isolated Fe^{3+} in T_h coordination or highly distorted O_h coordination. The later might be in the form of Fe^{3+} monomers that replace framework Al [34, 57, 61] or binuclear Fe-O-Fe species at cation exchange sites[62, 63], both represent active sites for high-temperature SCR. Furthermore, major fraction of Fe atoms form small Fe_2O_3 clusters that efficiently catalyze NH_3 oxidation[37, 38]. This likely results in lack of ammonia coordinated Cu^I complexes at high temperature under SCR conditions in the mixed catalyst as discussed in next section. The latter can suppress the activity of Cu-exchanged component in the high temperature SCR, but at the same time it should yield an improvement in N_2O selectivity of Cu-Fe-mix catalyst at high temperature SCR.

3.4 Cu-speciation upon activation and SCR

Cu K-edge XANES spectra consist of several distinct features indicative of the various electronic transitions for the Cu(I) and Cu(II) cations [64]. The peaks located at around 8977.0 eV and 8987.0 eV are representative of Cu(II) species. The first one is originated from the dipole-forbidden $1s \rightarrow 3d$ transition, which becomes allowed due to mixing of the 3*d* and 4*p* orbitals and has been reported in several studies as a low intensity pre-edge feature [65, 66]. The shoulder at 8987.0 eV is due to the $1s \rightarrow 4p$ electronic transition in Cu(II). The presence of the feature centered around 8983.0 eV is characteristic of the $1s \rightarrow 4p$ transition for a Cu(I) two-coordinated complexes in almost linear geometry (hereinafter referred to as Cu(I) rising-edge feature) [23, 24, 64]

The Cu K-edge XANES spectra collected in steady state condition upon activation in oxygen (gas feed 10% O_2 + 90% He) are reported in Figure 4. The gradual heating up to 200 °C results in the formation of Cu(I)/Cu(II) rising-edge shoulders. The developments of Cu(I) rising-edge feature is continued with the further temperature increase reaching a maximum at around ~ 400 °C (See Figure S15 of SI for more detailed T-driven evolution of Cu K-edge XANES upon activation).

Afterwards the intensity of Cu(I) rising edge shoulder starts to decrease denoting re-oxidation phase. XANES spectrum obtained for the O_2-activated Cu-CZC sample closely resemble the one recently reported by Kvande et. al. [67] for Cu-SAPO-34 with a very similar Cu loading and lower Si content (1.58 wt % Cu, Cu:Si = 0.25).

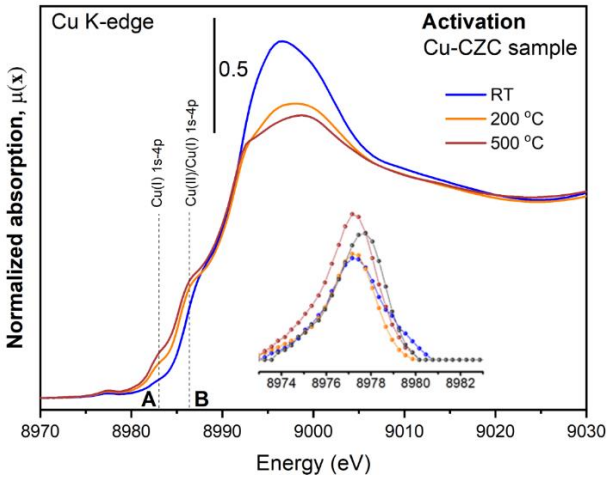

Fig. 4 Cu K-edge XANES spectra collected for monometallic Cu-CZC catalysts under steady-state conditions at RT, 200 °C and 500 °C upon the activation in oxygen. Vertical dashed lines corresponds to the position rising-edge features assotiated with $1s \rightarrow 4p$ transition in CuI (A) or CuII/CuI (B) configurations.

In accordance with the literature [25, 26, 68, 69], the Cu K-edge XANES collected both for monometallic Cu-CZC and mixed samples in hydrated state closely resemble those collected on a Cu(II)-acetate aqueous solution and hydrated Cu-exchanged Cu-SSZ-13 sample. Considering structural similarity of SAPO-34 and SSZ-13 frameworks, both monometallic Cu-CZC and Cu-Fe-mix samples undergo several stages upon high-temperature activation in oxygen: **(i)** *dehydration* (accompanied by drastic decrease in the intensity of WL peak and simultaneous developing of Cu(I) and Cu(I)/Cu(II) rising-edge features, denoted as feature A and B in Figure 4 **(ii)** *transient reduction* (characterized by gradual decrease of the WL peak intensity and maxima for Cu(I) rising-edge feature) followed by **(iii)** *Re-oxidation* (associated with notable loss of feature A intensity and minor restoration of WL peak intensity, see Figure S15 of SI). The stage (ii) takes place even in the abundant presence of oxidative agent such as oxygen [70, 71].

Considering previous works [25, 72-75] the final state in O_2-activated catalyst (See red curve in Figure 4) can be assigned to different framework-coordinated Cu-sites dominated by Cu^{II} oxo-species such as Z-Cu^{II}(OH) or Z-$Cu^{II}_xO_y$. Importantly, only small differences in Cu K-edge XANES and Fourier Transformed EXAFS amplitudes have been obtained between activated Cu-CZC and Cu-Fe-mix catalysts (See Figure S12 of SI). Hence further structural refinement of the Cu-sites in O_2-activated state is beyond of the scope of the present work. Moreover, the variety of different Cu-oxo species in the activated samples makes quantitative analysis of Cu K-edge EXAFS complicated. The example of multi-component fit for O_2-activated Cu-CHA is reported in our previous work [73]. Cu-speciation in monometallic Cu-exchanged zeolites under NH_3-SCR condition has been widely investigated [23, 28, 31, 72, 76]. Cu K-edge XANES spectra collected for monometallic Cu-CZC sample under NH_3-SCR conditions in wide temperature range are reported in Figure 5.

The spectra collected in the middle temperature range (i.e. 250 °C/300 °C) for Cu-CZC sample investigated in the present work (ca. 1.56 wt. % Cu, and Cu:Si ratio 0.44) demonstrate very similar XANES signal as reported for Cu-SAPO-34 (3.48 wt % Cu) by Doronkin et al. [45]. One observes raise of the characteristic Cu(I) rising-edge feature (located at ca. 8983.0 eV) with a temperature decrease that is reaching a maximum at 300 °C. Afterwards it starts to drop down with further

temperature decrease down to 150 °C. At low temperature range a significant increase of the WL peak intensity is observed due to approaching of the favorable conditions for re-hydration of the sample by water molecules present in the reaction feed. At 100 °C Cu-CZC sample is partially re-hydrated but a very weak contribution in the region of Cu(I) rising-edge feature remains in the spectra.

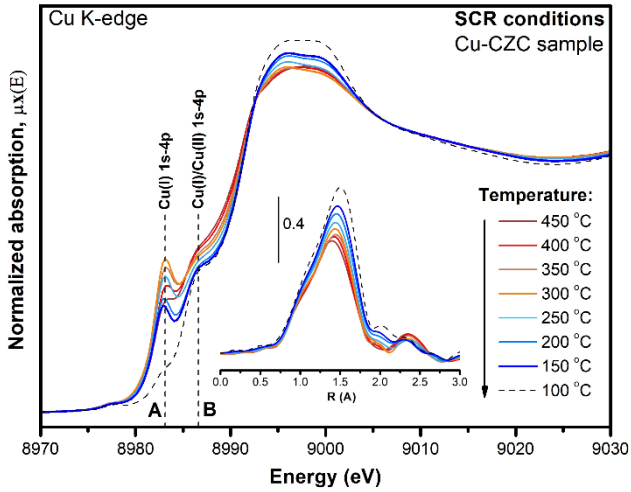

Fig. 5 Cu K-edge XANES spectra collected for monometallic Cu-CZC sample under steady-state NH_3-SCR reaction conditions at different temperatures.The inset demonstrates corresponding k^2-weighted phase uncorrected FT-EXAFS amplitudes.

The spectra collected in the middle temperature range (i.e. 250 °C/300 °C) for Cu-CZC sample investigated in the present work (ca. 1.56 wt. % Cu, and Cu:Si ratio 0.44) demonstrate very similar XANES signal as reported for Cu-SAPO-34 (3.48 wt % Cu) by Doronkin et al. [45]. One observes raise of the characteristic Cu(I) rising-edge feature (located at ca. 8983.0 eV) with a temperature decrease that is reaching a maximum at 300 °C. Afterwards it starts to drop down with further temperature decrease down to 150 °C. At low temperature range a significant increase of the WL peak intensity is observed due to approaching of the favorable conditions for re-hydration of the sample by water molecules present in the reaction feed. At 100 °C Cu-CZC sample is partially re-hydrated but a very weak contribution in the region of Cu(I) rising-edge feature remains in the spectra.

The temperature-driven behaviors of single-component Cu-CZC catalysts are in a good agreement with the previous studies on Cu-SSZ-13 catalyst [23, 28, 72]. In these studies, the development of Cu(I) rising-edge feature has been assigned to the formation of mobile linear di-amino complexes. Moreover, the lack of the intensity in the second shell region observed in EXAFS signal at low temperature range has been explained by the formation of ammonia solvated mobile complexes, including tetra-amino complexes [23] and recently reported mixed-ligand amino complexes [77].

As it was discussed above, the activated state of the Cu-CZC and Cu-Fe-mix samples yields very similar XANES and EXAFS signals (See Figure S12 of SI), declaring no significant changes in Cu-speciation upon high-temperature pre-treatment. Also, the evolution of the XANES spectra obtained for monometallic Cu-CZC sample under SCR conditions (as reported in a previous section) is in good agreement with previously reported data for Cu-SAPO-34 [45]. However, rather different Cu-speciation has been observed under reaction conditions for bimetallic Cu-Fe-mixed sample comparing to Cu-CZC for the whole temperature range, as shown in XANES and FT-EXAFS amplitudes reported on Figure 6. One observes that the most explicit differences between monometallic Cu-CZC and bimetallic Cu-Fe-mix samples reflected in the different intensity of

Cu(I) rising edge feature (located at *ca.* 8983.0 eV) as well as in the different intensity and shape of WL peak in the XANES part of the spectra (See Figure 6a).

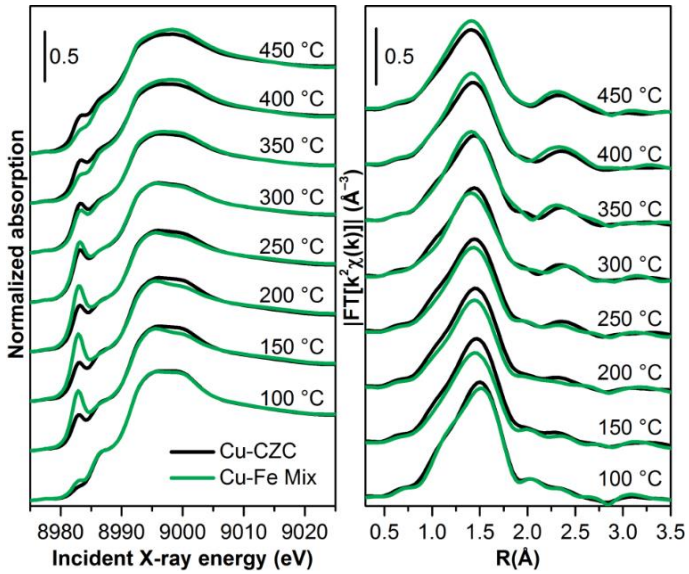

Fig. 6 (a) Normalized Cu K-edge XANES spectra and **(b)** k^2-weighted phase uncorrected FT-EXAFS amplitudes collected at different temperatures under NH_3-SCR conditions. Black and green curves correspond to monometallic Cu-CZC and bimetallic Cu-Fe-mixed catalysts, respectively.

Indeed, for the high temperature data collected at 450 °C (under NH_3-SCR conditions) Cu sites in Cu-CZC sample are notably more reduced with respect to Cu-Fe-mix sample. However, the situation drastically changes for temperatures below 300 °C, where the maximum of Cu(I) rising-edge intensity is observed for Cu-CZC (being already less developed compared to Cu-Fe-mix sample). For Cu-Fe-mix the 1s→4p Cu(I) rising-edge feature grows with the decrease of temperature (See Figure 6a), reaching maximum at 200 ℃ and revealing significant reduction of Cu-sites. At 150 ℃ it remains to be well developed for Cu-Fe- mixed sample (the intensity of this feature is still much higher than at 300 ℃, in contrast with Cu-CZC case). Even at 100 ℃ in the Cu(I) rising-edge region one could observe well-developed step-like shoulder for Cu-Fe-mixed sample, while it almost disappears for monometallic Cu-CZC.

In the EXAFS parts (See Figure 6b) at higher temperature range one clearly observes 2nd shell maxima both for Cu-CZC and Cu-Fe-mix samples which is, accordingly to the previously reported EXAFS findings[28], associated with the formation of framework coordinated Cu-oxo species Z-$Cu^{II}(OH)/O_2$ and nitrate species such as Z-$Cu^{II}(NO_3)$. In addition to the different abundancy of reduced mobile Cu(I) amino-complexes (proved by XANES), that obviously results in different intensity of the 1st shell maximum in FT-EXAFS signal (due to the lower coordination number for mobile di-amino complexes, CN=2), the most conspicuous difference observed for the temperature evolution of EXAFS signal under SCR conditions lies in the 2nd shell peak intensity evolution at the middle temperature range. Indeed, one can emphasize not negligible contribution to the 2nd shell maximum still observed for Cu-CZC at 250 ℃, whereas the signal obtained for Cu-Fe-mixed catalysts in this region lacks of intensity. As it was mentioned above, the quantitative EXAFS analysis is complicated because of the big variety of different Cu species that could be formed and contribute to the averaged EXAFS signal under reaction conditions [28, 72]

3.5 Quantification of Cu-species under reaction conditions

In this section, the relative abundancy of the different Cu-species is quantified under reaction conditions using XANES LCF (Linear Combination Fit) analysis. Based on the previously reported results on Cu-speciation under NH_3-SCR conditions [23, 28, 72] as well as on the advanced statistical analysis performed by means of SVD procedure (See Section 5.1 of SI) as implemented in PyFitit package [60], five principal components were used in order to reproduce each spectrum from the entire dataset. The details on statistical and PCA analysis as well as motivation for the selected reference spectra for LCF analysis are reported in Supporting Information. The results of LCF analysis are reported in Figure **7** (a-b). For the sake of simplicity, the contribution from two different framework coordinated complexes (Z-$Cu^{II}(OH)/O_2$ and Z-$Cu^{II}(NO_3)$) and two different Cu^I complexes ($Cu^I(NH_3)_2$ and $Cu^I(NH_3)O_{fw}$) were combined and labelled with Z-Cu(II) and Cu(I), while the mobile mixed ligand complex $Cu^{II}(NH_3)_3X$ is labelled with m-Cu(II) (the temperature profiles for all five principle components are reported in Figure S11 of SI).

One can see that at high temperature (400 °C and 450 °C) both monometallic Cu-CZC and bimetallic Cu-Fe-mixed samples dominated by the contributions from framework interacting Z-Cu(II) complexes, being slightly less abundant for Cu-CZC sample that is compensated by the higher concentration of framework interacting Z-Cu(I) complex. This result is in correlation with the lower magnitude of the 1st shell maximum in FT-EXAFS amplitudes (reported in Figure 6b) obtained at 400 °C and 450 °C for Cu-CZC sample with respect to the mixture. The lower reducibily of Cu sites in Cu-Fe-mix at high temperatures could be explained by the presence of small Fe_2O_3 clusters (likely formed on exterior surface of Fe-MOR) that effeciently catalize NH_3 oxidation [37, 38] and thus prevent the formation of Z-Cu(I) complexes.

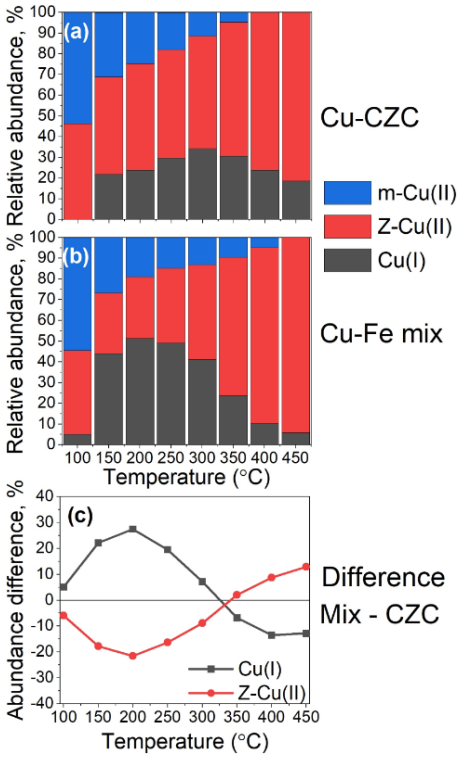

Figure 7 Relative abundance temperature profile for different Cu-species formed in the monometallic Cu-CZC **(a)** and mechanical mixture Cu-Fe-mix **(b)** catalysts under NH_3-SCR conditions, derived by XANES linear combination fit. **(c)** Difference in relative abundancy of framework-coordinated Z-Cu^{II} and Cu^I sites in mechanical mixture and monometallic Cu-CZC samples.

At T = 100 °C almost the same ratio between Z-Cu(II) and m-Cu(II) species accompanied by small contribution (below 5%) from the mobile Cu(I) species is observed for Cu-CZC and Cu-Fe-mix samples. As discussed above, the most significant difference in Cu-speciation between Cu-CZC and Cu-Fe mixture has been observed at low-medium temperatures.

4. Discussion

Overall, the temperature-driven behavior of different pure components demonstrates significantly higher abundancy of the mobile linear di-amino complexes at the low and medium temperature SCR for Cu-Fe-mixed catalyst with respect to pure copper catalyst Cu-CZC (See Figure **7**).

Figure **1**a represents conversion data collected upon the XAS operando experiment obtained by monitoring NO traces using MS spectrometry. MS data evidently demonstrate lower NO conversion for Cu-Fe-mixed sample in the low temperature range (T < 250 °C) with respect to monometallic copper catalysts. Considering for the very low NO conversion obtained for pure iron catalyst (~ 4.5% at 150 °C and ~ 16.5% at 200 °C) the Fe-MOR counterpart can be roughly considered as spectator in Cu-Fe-mix catalyst in low temperature range.

A direct interaction between Cu and Fe sites or the formation of any Cu-Fe conglomerates is excluded because no Cu-Fe interactions were evidenced by XANES or EXAFS analysis, both for Cu and Fe K-edges. The possible explanation of the different Cu-speciation is based on the fact that lower conversion observed for mechanical mixture may result in the scenario when Cu sites in Cu-Fe-mixed catalyst in average are exposed to the gas feed that contains more reactant molecules (namely, NH_3 and NO), with respect to the case of monometallic Cu-CZC catalyst. Such conditions are likely to be favourable for the higher reducibility of the Cu sites observed for the mixed catalyst. Indeed, recently Doronkin et al. [45] have shown the evolution of the Cu oxidation state along a capillary (by operando Cu K-edge XANES) at the fixed temperature and gas feed composition, exhibiting higher abundancy of Cu^{II} sites at downstream end of the capillary, where the copper ions are exposed to lean SCR gas mixture. Apparently, when the highly productive at low temperature region Cu-CZC catalyst is diluted by less active Fe-MOR counterpart an averaged oxidation state of Cu in the pellet can decrease, similarly to the capillary case described by Doronkin et al. [45].

Besides, low-temperature SCR mechanism recently proposed in the literature [31, 32 78] may contribute to the observed effect as well. It has been shown that a re-oxidation cycle at low temperature SCR may occur by the activation of oxygen through the dimerization reaction of two proximal mobile di-amino complexes [31, 32, 78], implying a pseudo-homogeneous character of the reaction.

Paolucci et al. demonstrated that the probability for the single $Cu^{I}(NH_3)_2$ to leave a resting cage is very high even at temperature as low as 200 °C, however its traveling capability is constrained by the electrostatic tethering to charge-compensating framework Al sites [31]. From the other side, the restricted migration mobility of di-amino complexes was proposed on the basis of transient reduction experiments [31], where the gas feed contains only 10% of O_2 balanced in He, while under SCR conditions the electrostatic tethering can be diminished by the termination of uncompensated Al sites by the protons (possibly delegated from water molecule) or both protons and NH_3 (forming an ammonium cation NH_4^+) with the formation of Brønsted acidic sites. Indeed, this mechanism might be very similar to the one recently elaborated for SSEI (Solid State Ion Exchange) on the DFT level by L. Chen et al. [79], that implies migration of NH_3-solvated di-amino complexes inside the zeolite structure, that is accompanied by the H^+ or NH_4^+ cation migration in

an opposite direction. Moreover, it was shown experimentally that NH_3-meadiated transfer of copper ions from the surface of Cu(I) oxide into zeolite frameworks may efficiently occur at the temperatures as low as 200-250 ^oC [23, 80] and that the simultaneous presence of NH_3 and NO molecules in a feed facilitate SSIE independently on the primary source of copper, i.e. Cu(I) or Cu(II) oxides [81-83].

In line with the above described SSEI migration mechanism, we can hypothesize that when Cu-CZC catalyst diluted by Fe-MOR counterpart, some fraction of NH_3-solvated di-amino complexes can gradually migrate from the SAPO-34 to MOR framework environment under SCR condition in low-medium temperature range - passing through the interface between different zeolite grains. This assumption is in good agreement with very recent work by H. Lee et al. [84], where inter-particle Cu migration were investigated for Cu-exchanged and protonated SSZ-13 prepared by simple mechanical mixing. It was shown that after hydrothermal aging the mixture of Cu-SSZ-13 and H-SSZ-13 behaves in a very similar way as Cu-SSZ-13 with two times lower Cu-content, assuming almost homogeneous distribution of Cu in the mixture. The SSEI and Cu migration upon hydrothermal aging for Cu-SAPO-34 are also reported elsewhere [85-87].

In our case the proposed migration phenomenon will gradually decrease the density of $Cu^I(NH_3)_2$ species in Cu-Fe-mix sample (with respect to those for monometallic copper zeolite) and increase the number of "uncoupled" di-amino complexes in mechanical mixture. It should eventually inhibit the oxygen activation via dimerization reaction and thus prevent re-oxidation of $Cu^I \rightarrow Cu^{II}$. Thus, the migration mechanism can be one of the reasons of higher abundance of reduced Cu^I sites in the Cu-Fe-mix sample below 250 ^oC (as reported in Figure **7**), where the major part of Cu(I) component is represented by mobile $Cu^I(NH_3)_2$ complexes. This higher abundance of reduced Cu^I sites might be also considered as a consequence of decreased efficiency in the oxidation of NO into NO_2 (only NO is fed and only NO_2 traces were detected in parallel laboratory IR experiment), which hinders the fast SCR reaction, so degrading the catalyst performance respect to the case when equimolar amounts of NO and NO_2 are fed among reactants.

With respect to the previously published results [22], some apparent discrepancies need to be addressed. First, the clear synergetic effects of the physical mixture appear less clear in the present work. There are a number of reasons for this.

First, in this work the catalysts systems are compared under standard SCR conditions, while fast SCR conditions were applied in [22], *i.e*. we use only NO, and not NO_2. In this work we observe depletion of the Cu concentration in Cu-CZC component as a part of Cu-Fe-mix sample because of the Cu migration. This mitigates especially the low temperature re-oxidation, which in turn is not affected to the same degree under fast SCR conditions.

Second, the different catalyst loadings employed due to the optimization of the XAS signals makes the comparative kinetic analysis more complex. In order to clarify this we have made a simple elaboration of the kinetic analysis based on pseudo first order derived kinetic constants, and thus compared the performance of the systems at GHSV 50.000 h^{-1} to exhibit the behavior under realistic conditions (See Figure 1 and Section 1 of SI). What is seen is that some synergetic effects are observed (See Figure 1), but they are less pronounced due to the use of standard SCR gas conditions and observed Cu migration.

Summarizing, we observe that the dilution of the monometallic Cu-CZC catalyst by the mixing with Fe-MOR (low-active towards NO conversion at the low-temperature SCR) results to the higher reducibility of the Cu sites in middle and low temperature SCR observed by operando XAS experiment.

The presence of the less active Fe-MOR can result in the gas feed in proximity of Cu-sites that has elevated concentration of NH_3 and NO. This will stimulate the migration process of NH_3-solvated mobile di-amino complexes from Cu-CZC to large pores Fe-MOR.

This copper migration eventually decreases the spatial density of mobile Cu^I complexes in the entire system, thus inhibiting the dimerization reaction - considered as a key step for the re-oxidation cycle of low-temperature SCR. This would result in higher reducibility of the Cu sites in the mixed sample, clearly observed by Cu K-edge XAS. From the other side this ionic migration process may results to the redistribution of copper sites forming more effective catalytic phase in the zeolite framework that resulted in synergetic effect observed for the first time in [22] and partially inhibited here by the specific reaction condition.

Furthermore, the detailed information derived from the XAS data in this study allows us to further suggest an optimization of such physical mixtures. In order to pre-compensate for the observed Cu loss due to migration, mixtures with less fraction of Fe-MOR and high fraction of Cu-CZC can be used (i.e. 70 % of Cu-CZC and 30 % of Fe-MOR). Note that the main synergetic effect and role of Fe-MOR is expected to be at high temperature where the activity and selectivity of Cu-CZC is lower. Above 300 ^oC kinetics are orders of magnitudes higher when selectivity is upheld as in the case of Fe-MOR. Thus, it would not be expected to be harmful for high temperature performance to use e.g. 30% Fe-MOR instead of 50% in the mixture that will be the subject of our further studies. In summary, the physical mixtures remain a very interesting and practical solution to achieve a complete temperature window for the SCR reaction, and this work helps understanding the precise speciation and thus provide future guidance to design of such systems.

5. Conclustions

The mechanical mixture (Cu-Fe-mixed), that has already showed superior activities than the monometallic exchanged zeolites[22], was prepared in a simple way by mixing Cu-exchanged (Cu-SAPO-34) and Fe-exchanged (Fe-MOR) catalysts. To understand the reason of this phenomenon, the monometallic and mixture catalysts were investigated by operando XAS spectroscopy under NH_3-SCR conditions in a wide temperature range.

The PXRD analysis evidences no traces of bulk metal oxides both in parent monometallic and mixed bimetallic catalysts. Fe K-edge XANES and EXAFS analysis shows that most of the iron species in Fe-MOR and Cu-Fe-mix samples exist in the form of small iron oxide cluster (beyond the detection limit of laboratory XRD) with a local atomic structure similar to bulk α-Fe_2O_3 (hematite phase). The cluster size was estimated as ~ 2.3 ± 0.6 nm by means of EXAFS fitting. The changes in the Fe K-edge EXAFS spectra observed both upon high temperature activation and under SCR conditions at different temperatures are mostly due to the temperature effect without any significant structural modifications. However, differential Fe K-edge XANES reveals the involvement of minority of isolated iron sites into redox chemistry in the high temperature SCR.

Analysis of Cu K-edge dataset acquired upon high temperature O_2-activation do not exhibit any significant changes between Cu-speciation in monometallic catalyst and mechanical mixture. However, dramatical differences were observed under reaction conditions, particularly in the low-temperature range. XANES LCF analysis clearly demonstrates that the presence of Fe-MOR component changes the Cu^I:Cu^{II} balance in the mechanical mixture declaring significantly higher abundance for mobile Cu^I di-amino complexes in the low temperature range. The latter, in principle could be considered as a reason of such different behavior of Cu-speciation simply accounting for higher availability of the reactant molecules (i.e. NO and NH_3 molecules) in

proximity of Cu sites for the Cu-Fe-mixed sample. Additionally, the dilution of Cu-CZC catalyst by the large-pores Fe-MOR may initiate gradual migration of mobile Cu^{I} complexes to MOR framework, similarly to SSIE mechanism, that will inhibit the oxygen activation via dimerization reaction (proposed as a key step for low-temperature SCR), thus preventing the re-oxidation step and yielding higher reducibility of Cu sites in mechanical mixture clearly observed by XAS. This work generates clear suggestions on how to circumvent this for the design of future SCR solution based on physical mixtures.

Conflicts of interest

There are no conflicts to declare.

Acknowledgements

The authors acknowledge ESRF (beamline BM23) for allocation of beamtime. The research was financially supported by the Ministry of Science and Higher Education of the Russian Federation (State assignment in the field of scientific activity, № 0852-2020-0019).

The authors declare no conflict of interests.

***

This work is dedicated to the memory of Prof. Carlo Lamberti. We will be always indebted to Carlo, for his constant support and brilliant guidance in the use of synchrotron ration to solve wide range of problems in catalysis. It is difficult to overestimate his contribution to the research dedicated to characterization of catalysts via *in situ* and *operando* synchrotron and laboratory experiments. We will always remember his unique enthusiasm in work and in everyday life.

Notes and references:

1. G. Busca, L. Lietti, G. Ramis and F. Berti, *Appl. Catal. B: Environ.*, 1998, **18**, 1-36.
2. P. Granger and V. I. Parvulescu, *Chem. Rev.*, 2011, **111**, 3155-3207.
3. E. Borfecchia, P. Beato, S. Svelle, U. Olsbye, C. Lamberti and S. Bordiga, *Chem. Soc. Rev. ACS*, 2018, **47**, 8097-8133.
4. D. Chatterjee and K. Rusch, in *Urea-SCR Technology for deNOx After Treatment of Diesel Exhausts*, eds. I. Nova and E. Tronconi, Springer New York, New York, NY, 2014, pp. 33-61.
5. I. Nova and E. Tronconi, *Urea-SCR Tehcnology for deNOx after treatment of diesel exhausts*, Springer-Verlag New York, New Your, NY, 2014.
6. R. Zhang, N. Liu, Z. Lei and B. Chen, *Chem. Rev.*, 2016, **116**, 3658-3721.
7. P. S. Metkar, M. P. Harold and V. Balakotaiah, *Chem. Eng. Sci.*, 2013, **87**, 51-66.
8. M. Colombo, I. Nova and E. Tronconi, *Catal. Today*, 2010, **151**, 223-230.
9. A. Sultana, M. Sasaki, K. Suzuki and H. Hamada, *Catal. Commun.*, 2013, **41**, 21-25.
10. D. Wang, L. Zhang, J. Li, K. Kamasamudram and W. S. Epling, *Catal. Today*, 2014, **231**, 64-74.
11. D. W. Fickel, E. D'Addio, J. A. Lauterbach and R. F. Lobo, *Appl. Catal.B-Environ.*, 2011, **102**, 441-448.
12. F. Gao, Y. Wang, M. Kollár, N. M. Washton, J. Szanyi and C. H. F. Peden, *Catal. Today*, 2015, **258**, 347-358.
13. A. Shishkin, S. Shwan, T. N. Pingel, E. Olsson, A. Clements, P.-A. Carlsson, H. Harelind and M. Skoglundh, *Catalysts*, 2017, **7**, 232.
14. H. Zhao, H. Li, X. Li, M. Liu and Y. Li, *Catal. Today*, 2017, **297**, 84-91.
15. O. Kröcher and M. Elsener, *Ind. Eng. Chemi. Res.*, 2008, **47**, 8588-8593.
16. Y. Teraoka, H. Ogawa, H. Furukawa and S. Kagawa, *Catal. Lett.*, 1992, **12**, 361-366.
17. A. L. Kustov, E. E. Knyazeva, E. A. Zhilinskaya, A. Aboukais and B. V. Romanovsky, in *Studies in Surface Science and Catalysis*, eds. A. Galarneau, F. Fajula, F. Di Renzo and J. Vedrine, Elsevier, 2001, vol. 135, p. 350.
18. A. V. Kucherov, D. E. Doronkin, A. Y. Stakheev, A. L. Kustov and M. Grill, *J. Mol. Catal. A Chem.*, 2010, **325**, 73-78.

19. C. Hammond, R. L. Jenkins, N. Dimitratos, J. A. Lopez-Sanchez, M. H. ab Rahim, M. M. Forde, A. Thetford, D. M. Murphy, H. Hagen, E. E. Stangland, J. M. Moulijn, S. H. Taylor, D. J. Willock and G. J. Hutchings, *Chem.-Eur. J.*, 2012, **18**, 15735-15745.
20. C. Hammond, M. M. Forde, M. H. Ab Rahim, A. Thetford, Q. He, R. L. Jenkins, N. Dimitratos, J. A. Lopez-Sanchez, N. F. Dummer, D. M. Murphy, A. F. Carley, S. H. Taylor, D. J. Willock, E. E. Stangland, J. Kang, H. Hagen, C. J. Kiely and G. J. Hutchings, *Angew. Chem. Int. Ed. Engl.*, 2012, **51**, 5129-5133.
21. P. Boroń, L. Chmielarz and S. Dzwigaj, *Appl Catal B-Environ.*, 2015, **168-169**, 377-384.
22. H. I. Hamoud, V. Valtchev and M. Daturi, *Appl Catal B-Environ.*, 2019, **250**, 419-428.
23. T. V. W. Janssens, H. Falsig, L. F. Lundegaard, P. N. R. Vennestrøm, S. B. Rasmussen, P. G. Moses, F. Giordanino, E. Borfecchia, K. A. Lomachenko, C. Lamberti, S. Bordiga, A. Godiksen, S. Mossin and P. Beato, *ACS Catal.*, 2015, **5**, 2832-2845.
24. F. Giordanino, E. Borfecchia, K. A. Lomachenko, A. Lazzarini, G. Agostini, E. Gallo, A. V. Soldatov, P. Beato, S. Bordiga and C. Lamberti, *J. Phys. Chem. Lett.*, 2014, **5**, 1552-1559.
25. E. Borfecchia, K. A. Lomachenko, F. Giordanino, H. Falsig, P. Beato, A. V. Soldatov, S. Bordiga and C. Lamberti, *Chem. Sci.*, 2015, **6**, 548-563.
26. F. Giordanino, P. N. Vennestrom, L. F. Lundegaard, F. N. Stappen, S. Mossin, P. Beato, S. Bordiga and C. Lamberti, *Dalton Trans.*, 2013, **42**, 12741-12761.
27. C. W. Andersen, E. Borfecchia, M. Bremholm, M. Jørgensen, P. Vennestrøm, C. Lamberti, L. Lundegaard and B. Brummerstedt Iversen, *Angew. Chem. Int. Ed. Engl.*, 2017, **56**, 10367-10372.
28. K. A. Lomachenko, E. Borfecchia, C. Negri, G. Berlier, C. Lamberti, P. Beato, H. Falsig and S. Bordiga, *J. Am. Chem. Soc.*, 2016, **138**, 12025-12028.
29. C. Tyrsted, E. Borfecchia, G. Berlier, K. A. Lomachenko, C. Lamberti, S. Bordiga, P. N. R. Vennestrøm, T. V. W. Janssens, H. Falsig, P. Beato and A. Puig-Molina, *Catal. Sci. Technol.*, 2016, **6**, 8314-8324.
30. A. Kato, S. Matsuda, T. Kamo, F. Nakajima, H. Kuroda and T. Narita, *Am. J. Phys. Chem.*, 1981, **85**, 4099-4102.
31. C. Paolucci, I. Khurana, A. A. Parekh, S. C. Li, A. J. Shih, H. Li, J. R. Di Iorio, J. D. Albarracin-Caballero, A. Yezerets, J. T. Miller, W. N. Delgass, F. H. Ribeiro, W. F. Schneider and R. Gounder, *Science*, 2017, **357**, 898-903.
32. F. Gao, D. Mei, Y. Wang, J. Szanyi and C. H. F. Peden, *Journal of the American Chemical Society*, 2017, **139**, 4935-4942.
33. F. Heinrich, C. Schmidt, E. Löffler, M. Menzel and W. Grünert, *J. Catal.*, 2002, **212**, 157-172.
34. M. Iwasaki, K. Yamazaki, K. Banno and H. Shinjoh, *J. Catal.*, 2008, **260**, 205-216.
35. M. M. Forde, R. D. Armstrong, R. McVicker, P. P. Wells, N. Dimitratos, Q. He, L. Lu, R. L. Jenkins, C. Hammond, J. A. Lopez-Sanchez, C. J. Kiely and G. J. Hutchings, *Chem. Sci.*, 2014, **5**, 3603-3616.
36. F. Gao, M. Kollár, R. K. Kukkadapu, N. M. Washton, Y. Wang, J. Szanyi and C. H. F. Peden, *Appl Catal B-Environ.*, 2015, **164**, 407-419.
37. M. S. Kumar, M. Schwidder, W. Grünert and A. Brückner, *J. Catal.*, 2004, **227**, 384-397.
38. M. S. Kumar, M. Schwidder, W. Grünert, U. Bentrup and A. Brückner, *J. Catal.*, 2006, **239**, 173-186.
39. S. H. Choi, B. R. Wood, J. A. Ryder and A. T. Bell, *J. Phys. Chem. B*, 2003, **107**, 11843-11851.
40. M. Schwidder, M. S. Kumar, K. Klementiev, M. M. Pohl, A. Brückner and W. Grünert, *J. Catal.*, 2005, **231**, 314-330.
41. S. M. Maier, A. Jentys, E. Metwalli, P. Müller-Buschbaum and J. A. Lercher, *J. Phys. Chem. Lett.*, 2011, **2**, 950-955.
42. G. I. Panov, G. A. Sheveleva, A. S. Kharitonov, V. N. Romannikov and L. A. Vostrikova, *Appl. Catal. A: Gen.*, 1992, **82**, 31-36.
43. A. A. Battiston, J. H. Bitter, W. M. Heijboer, F. M. F. de Groot and D. C. Koningsberger, *J. Catal.*, 2003, **215**, 279-293.
44. A. A. Battiston, J. H. Bitter and D. C. Koningsberger, *J. Catal.*, 2003, **218**, 163-177.
45. D. E. Doronkin, M. Casapu, T. Günter, O. Müller, R. Frahm and J.-D. Grunwaldt, *J. Phys. Chem. C*, 2014, **118**, 10204-10212.
46. J. Du, X. Shi, Y. Shan, Y. Wang, W. Zhang, Y. Yu, W. Shan and H. He, *Catal. Sci. Technol.*, 2020, **10**, 2855-2863.
47. O. Mathon, A. Beteva, J. Borrel, D. Bugnazet, S. Gatla, R. Hino, I. Kantor, T. Mairs, M. Munoz, S. Pasternak, F. Perrin and S. Pascarelli, *J. Synchrot. Radiat.*, 2015, **22**, 1548-1554.
48. B. Ravel and M. Newville, *J. Synchrot. Radiat.*, 2005, **12**, 537-541.
49. K. Klementiev and R. Chernikov, *J. Phys. Conf. Ser*, 2016, **712**, 012008.
50. F. de Groot, G. Vankó and P. Glatzel, *J. Phys. Condens. Matter*, 2009, **21**, 104207.

51. M. Wilke, F. o. Farges, P.-E. Petit, G. E. Brown, Jr. and F. o. Martin, *Am. Mineral*, 2001, **86**, 714-730.
52. H. Aritani, S. Nishimura, M. Tamai, T. Yamamoto, T. Tanaka and A. Nakahira, *Chem. Mater.*, 2002, **14**, 562-567.
53. A. Kuzmin and J. Chaboy, *IUCrJ*, 2014, **1**, 571-589.
54. R. E. H. R. L. Blake, T. Zoltai, L. W. Finger, *Am. Mineral.*, 1966, **51**, 123-129.
55. S. Calvin, M. M. Miller, R. Goswami, S.-F. Cheng, S. P. Mulvaney, L. J. Whitman and V. G. Harris, *Int. J. Appl. Phys.*, 2003, **94**, 778-783.
56. S. Calvin, S. X. Luo, C. Caragianis-Broadbridge, J. K. McGuinness, E. Anderson, A. Lehman, K. H. Wee, S. A. Morrison and L. K. Kurihara, *Appl. Phys. Lett.*, 2005, **87**, 233102.
57. M. Høj, M. J. Beier, J.-D. Grunwaldt and S. Dahl, *Appl Catal B-Environ.*, 2009, **93**, 166-176.
58. L. Kovarik, N. M. Washton, R. Kukkadapu, A. Devaraj, A. Wang, Y. Wang, J. Szanyi, C. H. F. Peden and F. Gao, *ACS Catalysis*, 2017, **7**, 2458-2470.
59. F. Gao, J. Szanyi, Y. Wang, B. Schwenzer, M. Kollár and C. H. F. Peden, *Top. Catal.*, 2016, **59**, 882-886.
60. A. Martini, S. A. Guda, A. A. Guda, G. Smolentsev, A. Algasov, O. Usoltsev, M. A. Soldatov, A. Bugaev, Y. Rusalev, C. Lamberti and A. V. Soldatov, *Comput. Phys. Commun.*, 2019, 107064.
61. P. Sánchez-López, Y. Kotolevich, E. Khramov, R. K. Chowdari, M. A. Estrada, G. Berlier, Y. Zubavichus, S. Fuentes, V. Petranovskii and F. Chávez-Rivas, *Catalysts*, 2020, **10**, 1156.
62. S. M. Maier, A. Jentys, M. Janousch, J. A. van Bokhoven and J. A. Lercher, *J. Phys. Chem. C.*, 2012, **116**, 5846-5856.
63. H. Xia, K. Sun, Z. Liu, Z. Feng, P. Ying and C. Li, *J. Catal.*, 2010, **270**, 103-109.
64. L. S. Kau, D. J. Spirasolomon, J. E. Pennerhahn, K. O. Hodgson and E. I. Solomon, *J. Am. Chem. Soc.*, 1987, **109**, 6433-6442.
65. C. Lamberti, S. Bordiga, M. Salvalaggio, G. Spoto, A. Zecchina, F. Geobaldo, G. Vlaic and M. Bellatreccia, *J. Phys. Chem. B.*, 1997, **101**, 344-360.
66. M. H. Groothaert, J. A. van Bokhoven, A. A. Battiston, B. M. Weckhuysen and R. A. Schoonheydt, *J. Am. Chem. Soc.*, 2003, **125**, 7629-7640.
67. K. Kvande, D. K. Pappas, M. Dyballa, C. Buono, M. Signorile, E. Borfecchia, K. A. Lomachenko, B. Arstad, S. Bordiga, G. Berlier, U. Olsbye, P. Beato and S. Svelle, *Catalysts*, 2020, **10**, 191.
68. K. A. Lomachenko, E. Borfecchia, S. Bordiga, A. V. Soldatov, P. Beato and C. Lamberti, *J. Phys. Conf. Ser*, 2016, **712**, 012041.
69. G. T. Palomino, S. Bordiga, A. Zecchina, G. L. Marra and C. Lamberti, *J. Phys. Chem. B.*, 2000, **104**, 8641-8651.
70. V. L. Sushkevich and J. A. van Bokhoven, *Chem. Commun.*, 2018, **54**, 7447-7450.
71. V. L. Sushkevich, A. V. Smirnov and J. A. van Bokhoven, *J. Phys. Chem. C*, 2019, **123**, 9926-9934.
72. C. Paolucci, A. A. Parekh, I. Khurana, J. R. Di Iorio, H. Li, J. D. Albarracin Caballero, A. J. Shih, T. Anggara, W. N. Delgass, J. T. Miller, F. H. Ribeiro, R. Gounder and W. F. Schneider, *J. Am. Chem. Soc.*, 2016, **138**, 6028-6048.
73. A. Martini, E. Borfecchia, K. A. Lomachenko, I. A. Pankin, C. Negri, G. Berlier, P. Beato, H. Falsig, S. Bordiga and C. Lamberti, *Chem. Sci.*, 2017, **8**, 6836-6851.
74. I. A. Pankin, A. Martini, K. A. Lomachenko, A. V. Soldatov, S. Bordiga and E. Borfecchia, *Catal. Today*, 2019.
75. D. K. Pappas, E. Borfecchia, M. Dyballa, I. A. Pankin, K. A. Lomachenko, A. Martini, M. Signorile, S. Teketel, B. Arstad, G. Berlier, C. Lamberti, S. Bordiga, U. Olsbye, K. P. Lillerud, S. Svelle and P. Beato, *J. Am. Chem. Soc.*, 2017, **139**, 14961-14975.
76. U. Deka, A. Juhin, E. A. Eilertsen, H. Emerich, M. A. Green, S. T. Korhonen, B. M. Weckhuysen and A. M. Beale, *J. Phys. Chem. C.*, 2012, **116**, 4809-4818.
77. C. Negri, E. Borfecchia, M. Cutini, K. A. Lomachenko, T. V. W. Janssens, G. Berlier and S. Bordiga, *ChemCatChem*, 2019, **11**, 3555-3555.
78. L. Chen, H. Falsig, T. V. W. Janssens and H. Grönbeck, *J. Catal.*, 2018, **358**, 179-186.
79. L. Chen, J. Jansson, M. Skoglundh and H. Grönbeck, *J. Phys. Chem. C*, 2016, **120**, 29182-29189.
80. M. Kögel, V. H. Sandoval, W. Schwieger, A. Tissler and T. Turek, *Catalysis Letters*, 1998, **51**, 23-25.
81. A. Y. Stakheev, D. A. Bokarev, A. I. Mytareva, T. V. W. Janssens and P. N. R. Vennestrøm, *Top. Catal.*, 2017, **60**, 255-259.
82. S. Shwan, M. Skoglundh, L. F. Lundegaard, R. R. Tiruvalam, T. V. W. Janssens, A. Carlsson and P. N. R. Vennestrøm, *ACS Catal.*, 2015, **5**, 16-19.

83. A. K. S. Clemens, A. Shishkin, P. A. Carlsson, M. Skoglundh, F. J. Martínez-Casado, Z. Matěj, O. Balmes and H. Härelind, *ACS Catal.*, 2015, **5**, 6209-6218.
84. H. Lee, I. Song, S. W. Jeon and D. H. Kim, *React. Chem. Eng.*, 2019, **4**, 1059-1066.
85. F. Gao, E. D. Walter, N. M. Washton, J. Szanyi and C. H. F. Peden, *Appl. Catal. B-Environ.*, 2015, **162**, 501-514.
86. X. Li, Y. Zhao, H. Zhao, M. Liu, Y. Ma, X. Yong, H. Chen and Y. Li, *Catal. Today*, 2019, **327**, 126-133.
87. X. Liu, X. Wu, D. Weng, Z. Si and R. Ran, *Catal. Today*, 2017, **281**, 596-604.